photonics

Article

Transmission of Vortex Solitons in Three-Dimensional $\chi^{(2)}$ Helical-Periodically Poled Ferroelectric Crystals

Yixi Chen [1], Aowei Yang [1], Yangui Zhou [1,2], Hexiang He [1,2,*] and Jianing Xie [1,2,*]

[1] School of Physics and Optoelectronic Engineering, Foshan University, Foshan 528000, China; fosucyx@163.com (Y.C.); aowei_yang@126.com (A.Y.); zygsai@163.com (Y.Z.)
[2] Guangdong-Hong Kong-Macao Joint Laboratory for Intelligent Micro-Nano Optoelectronic Technology, Foshan University, Foshan 528000, China
* Correspondence: sysuhhx@163.com (H.H.); xiejianingfs@126.com (J.X.)

Abstract: It is well known that bright vortex solitons are unstable in the $\chi^{(2)}$ nonlinear media due to the strong azimuthal modulation instability. To solve this problem, a quadratic ($\chi^{(2)}$) $LiNbO_3$ ferroelectric crystal with a special kind of helical-periodically poled structure is proposed. The proposed structure is designed by embedding topological charges into the crystal with a quasi-phase matching technique. Simulation results indicate that vortex solitons containing fundamental-frequency and second-harmonic waves can robustly propagate over a distance. Two types of vortex states are obtained: *double vortices* state and *vortex–antivortex* state. The dependence of effective area, propagation constants, and maximum light intensity on the control parameters are presented. These results provide a new solution for robust transmission of bright vortex solitons in a $\chi^{(2)}$ nonlinear media.

Keywords: vortex solitons; quasi-phase matching; quadratic nonlinear effect; helical-periodically poled lithium niobate

check for updates

Citation: Chen, Y.; Yang, A.; Zhou, Y.; He, H.; Xie, J. Transmission of Vortex Solitons in Three-Dimensional $\chi^{(2)}$ Helical-Periodically Poled Ferroelectric Crystals. *Photonics* **2023**, *10*, 818. https://doi.org/10.3390/photonics10070818

Received: 23 May 2023
Revised: 1 July 2023
Accepted: 11 July 2023
Published: 13 July 2023

1. Introduction

Nonlinear frequency conversion is an important nonlinear process that can generate new frequency components through nonlinear polarization interactions between light waves and media. It has attracted wide attention for its applications in resonant nanophotonics [1], sum-frequency generation spectroscopy [2], quantum information processing [3], etc. To achieve nonlinear frequency conversion, the momentum conservation condition is crucial. However, it is usually violated due to the dispersion effects in materials. Therefore, the phase matching technique should be introduced to realize highly efficient nonlinear frequency conversion. One of the popular phase matching techniques is to make use of the birefringent effect of a crystal to satisfy the momentum conservation condition [4–6]. However, it has high requirements on the incident angle, crystal orientation, etc., and makes it difficult to use the maximum nonlinear coefficient of the crystal [7]. Another promising phase-matching technique that excludes the disadvantages mentioned above is the quasi-phase matching (QPM) technique. Although it was proposed in advance of the birefringent phase matching technique [8], it has not been widely used until recently [9,10]. By periodically changing the polarization state in a bulk nonlinear crystal, a kind of nonlinear photonic crystal can be created with the QPM technique. It is attracting more and more attention with the rapid development of this regime [11–14]. In 2019, three-dimensional nonlinear photonic crystals were fabricated in lithium niobate crystals using femtosecond-laser-engineering techniques [15], which show great potential in shaping nonlinear processes. The radiation-induced optical absorption and phase-mismatch for third-order QPM second harmonic generation (SHG) in congruent $LiNbO_3$ crystals were subsequently investigated [16]. High-efficiency third-harmonic generation is achieved by designing an inhomogeneous QPM structure in a quadratic crystal using a Monte Carlo algorithm [17]. Multiplexing linear and nonlinear Bragg diffractions through volume gratings fabricated by femtosecond laser writing in lithium niobate crystals was reported recently [18]. Additionally, a theoretical study on mid-infrared difference frequency generation (DFG) based on periodically-poled thin-film lithium niobate was conducted in [19]. Bistable switching, adiabatic geometric phasing, Stern–Gerlach, and optical solitons [20,21] are some of the current interesting research topics in the field of nonlinear photonic crystals. In this letter, optical solitons are mainly studied.

As the knowledge in the field of optical solitons increases, the more complex solitons are studied. Among them, vortex solitons are particularly typical. Vortex solitons with vorticity are nonlinear modes that have been extensively investigated in fields such as nonlinear optics and Bose–Einstein condensates (BECs) in ultracold atomic gases [22,23]. There are various applications for vortex optical solitons that carry topological charges, such as light manipulation [24], optical tweezers [25], and quantum communication [26–28]. Fundamental solitons in quadratic ($\chi^{(2)}$) media can stably exist in free space [29–32]. However, vortex optical solitons with embedded vorticity will decay into low-order solitons (fundamental solitons) during propagation because of the instable azimuthal modulation [33–35]. In order to obtain stable vortex optical solitons, a common approach is to introduce competing nonlinearities [36–40]. In this way, stable 2D vortex optical solitons have been observed experimentally [41]. Additionally, competitive nonlinear phenomena can also be found in a BEC system for investigating vortex self-localized states and the formation of quantum droplets [42–46]. However, these competing nonlinearities rely on a high-power light source, and the effect of it is relatively weak. Another method to achieve stable vortex solitons is to introduce a spatially uniform lossy background and a ring-shaped gain in a $\chi^{(2)}$ medium [47]. It is reported that rhombus and square vortex optical solitons can be obtained in nonlinear photonic crystals with a checkerboard structure by the QPM technique [48]. Therefore, generating stable vortex optical solitons in pure $\chi^{(2)}$ media is proved to be feasible and valid. However, QPM crystals with a checkerboard structure, as in Reference [48], result in the intensity distribution of the vortex solitons having a four-peak profile rather than a ring-shaped profile. Additionally, these vortex solitons only exist in the fundamental-frequency (FF) component, while the second-harmonic (SH) component exhibits quadrupole mode behavior. Thus, the problems of vortex soliton splitting and the possibility of generating vortex soliton modes in both the FF and SH components remain intriguing and worth further investigation. Recent research reported that vortex beams can be generated directly through a nonlinear process by introducing a spiral periodic polarization structure in a ferroelectric crystal [49,50]. Inspired by this concept, a new method to generate vortex solitons is proposed. Specifically, spiral periodic polarization in a ferroelectric crystal structure is introduced so as to embed the topological charge in the $\chi^{(2)}$ crystal. By this method, accurate phase matching of the second harmonic process is ensured according to the QPM condition. Simulation results show that quasi-stable vortex optical solitons can be formed in realistic parameter space. Two types of vortex states are obtained: *double vortices* states and *vortex–antivortex* states. The relations of effective area, propagation constants, maximum light intensity with the input power, and effective detuning are discussed. It is proved to be a new method for stabilizing optical vortex solitons in a pure $\chi^{(2)}$ medium.

2. Theory and Model

In this study, quadratic solitons in the process of second harmonic generation are investigated. The structure of the nonlinear crystal is designed by the QPM technique. The coupled equations under the slowly varying amplitude approximation of this process are as follows:

$$i\partial_z A_1 = -\frac{1}{2k_1}\nabla^2 A_1 - \frac{2d(r,\theta,z)\omega_1}{cn_1}A_1^* A_2 e^{-i\Delta kz}, \tag{1}$$

$$i\partial_z A_2 = -\frac{1}{2k_2}\nabla^2 A_2 - \frac{d(r,\theta,z)\omega_2}{cn_2}A_1^2 e^{i\Delta kz}. \tag{2}$$

where the amplitude of FF and SH waves are denoted by A_1, A_2, respectively. $\nabla^2 = \partial_x^2 + \partial_y^2 = \partial_r^2 + r^{-1}\partial_r + r^{-2}\partial_\theta^2$ is the paraxial-diffraction Laplacian. The speed of light in a vacuum is c. $k_{1,2}$, $n_{1,2}$, and $\omega_{1,2}$ ($\omega_2 = 2\omega_1$) are the carrier wavenumbers, refractive indices, and frequencies of FF and SH waves, respectively. The phase mismatch between two waves is defined by $\Delta k = 2k_1 - k_2$. $d(r, \theta, z)$ is a modulation coefficient that characterizes the spatially varying magnitude of the $\chi^{(2)}$ susceptibility. It can be represented by the Fourier series expansion as:

$$d(r,\theta,z) = d_{\text{eff}} \sum_{m \neq 0} \frac{2}{m\pi} \sin[m\pi D] \exp\{im[Kz + \phi_d(r,\theta)]\}. \tag{3}$$

where $K = 2\pi/\Lambda$ (Λ is the modulation period) is the modulation wave-vector of the QPM and the duty cycle D is set to 1/2. d_{eff} represents the corresponding component of the $\chi^{(2)}$ susceptibility tensor, and $\phi_d(r,\theta)$ is the modulation phase factor created by a spatial function with a helical-periodically poled structure. Specifically, we set $\phi_d = n \cdot \theta (n = \pm 1, \pm 2, ...)$, which is equivalent to embedding the topological charges in a ferroelectric crystal. It is proved that this Fourier series expansion provides a specific representation of the helical periodic polarization structure in cylindrical coordinates (r, θ, z). The phase factor ϕ_d serves as a modulation phase factor, where the magnitude of the index, n, determines the degree of distortion in the ferroelectric crystal. Through this phase-twisted modulation, a helical periodic polarized ferroelectric crystal can be formed. Subsequently, we restrict our analysis to the fundamental harmonics associated with $m = 1$ and $m = -1$ in Equations (1) and (2), respectively, as they reflect the domain effect of the QPM.

By utilizing the definitions introduced in References [51,52], the following equations are derived:

$$I_0 = \sum_{j=1}^{2} \frac{n_j}{\omega_j} |A_0|^2, \tag{4}$$

$$\Psi_j = A_j \sqrt{\frac{n_j}{\omega_j I_0}} \exp[i(\Delta k - K)z], j = 1, 2, \tag{5}$$

$$z_d^{-1} = \frac{2d_{\text{eff}}\omega_1}{\pi c n_1} \sqrt{\frac{\omega_2}{n_2} I_0}, \tag{6}$$

$$Z = z/z_d, R = r\sqrt{k_1/z_d}, \tag{7}$$

$$\Delta\Gamma = z_d(\Delta k - K). \tag{8}$$

Here A_0 denotes a characteristic amplitude of the electromagnetic field, while $\Delta\Gamma$ represents the effective detuning. To simplify the analysis, Equations (1) and (2) are normalized by disregarding the material-dependent difference between n_1 and n_2. Additionally, by truncating the Fourier series expansion in Equation (3), the following expressions are derived:

$$i\partial_Z \Psi_1 = -\frac{1}{2}\nabla^2 \Psi_1 - \Delta\Gamma\Psi_1 - 2e^{i\phi_d(R,\theta)} \Psi_1^* \Psi_2, \tag{9}$$

$$i\partial_Z \Psi_2 = -\frac{1}{4}\nabla^2 \Psi_2 - \Delta\Gamma\Psi_2 - e^{-i\phi_d(R,\theta)} \Psi_1^2, \tag{10}$$

where $\nabla^2 = \partial_X^2 + \partial_Y^2 = \partial_R^2 + R^{-1}\partial_R + R^{-2}\partial_\theta^2$. Equations (9) and (10) possess a dynamical invariant. The total power (also known as the Manley-Rowe invariant [53]) is,

$$P = \iint (|\Psi_1|^2 + 2|\Psi_2|^2) dXdY \equiv P_1 + P_2. \tag{11}$$

The input power P, the effective detuning $\Delta\Gamma$, and the modulation phase factor ϕ_d are the control parameters of the system.

The bright vortex solitons of Equations (9) and (10) can be expressed as

$$\Psi_1(X,Y,Z) = \psi_1(X,Y)\exp(i\beta Z), \tag{12}$$
$$\Psi_2(X,Y,Z) = \psi_2(X,Y)\exp(2i\beta Z), \tag{13}$$

where ψ_1 and ψ_2 are the stationary shape of the FF and SH components, respectively. The propagation constants of them are β and 2β, respectively. The phase matching conditions of Equations (9) and (10) are given by:

$$\varphi_2 = 2\varphi_1 - \phi_d. \tag{14}$$

As mentioned previously, $\phi_d = n \cdot \theta (n = \pm1, \pm2, ...)$, which implies that vortex solitons with different topological charges can exist when n takes different integer values. The sign of n represents the rotation direction of the vortex soliton. By satisfying the phase matching conditions, we can achieve the effect of embedding topological charges in the crystal. If we set $\phi_d = \theta$ (namely $n = 1$), then the lowest solution of the phase matching conditions can be represented as:

$$\varphi_1 = \varphi_2 = \theta. \tag{15}$$

The resulting topological charges of two vortex solitons are $S_1 = S_2 = +1$, which leads to a *double vortices* states with identical directions of rotation. By setting $\phi_d = 3\theta$, the lowest solution of the phase matching conditions can be expressed as:

$$\varphi_1 = -\varphi_2 = \theta. \tag{16}$$

The resulting topological charges of the two vortex solitons are $S_1 = -S_2 = +1$, leading to a special type of vortex state called the *vortex–antivortex* state (also known as *hidden vortices* [42,43]). The numerical simulation results of these states will be extensively discussed in Section 3. It is worth noting that various states can be obtained for different integer values of n, which were not discussed in this paper. For instance, when $n = 6$ and $n = 9$, the lowest solutions are $S_{1,2} = \pm2$ and $S_{1,2} = \pm3$, respectively. These matching conditions correspond to *vortex–antivortex* solitons with high angular momentum. By varying the value of n, three distinct combinations of high-order vortices can be obtained: equal topological charges in both components, opposite topological charges in the two components, and unequal absolute values of the topological charges in the two components. In special cases, it is possible to achieve a topological charge value of zero in one component, allowing for the generation of the vortex state or elimination of the vortex state. Thus, it can be proved that under the condition of phase matching, the transformation of high-order topological charges between two components can be realized. Therefore, it has significant implications for the design of data storage devices or converters based on optical vortices, where information is encoded in the topological charges. Recently, in the study of quasi-two-dimensional *hidden vortices* of Bose–Bose mixture condensates trapped by thicker transverse confinement, *quantum droplets* with high angular momentum, having topological charges reaching up to $S = 4$, have been observed [54].

To estimate the physical parameters of the model, we assumed that the nonlinear photonic crystal is made by $LiNbO_3$. Then, the relevant parameters were set to: $d_{\text{eff}} = 27$ pm/V and $n_1 \approx n_2 \approx 2.2$. The wavelengths of FF and SH waves were selected as 1064 nm and 532 nm, respectively. According to Reference [30], the electric field amplitude A_0 in Equation (4) was set to be 50 kV/cm. The estimated relationships between the scaled units in Equations (9) and (10) and their physical counterparts are summarized in Table 1.

Table 1. The conversion relationship between dimensionless units and physical units.

$z = 1, \Delta\Gamma = 1$	0.25 cm, 4 cm^{-1}
$x = 1, y = 1$	14 μm
$\lvert\Psi_1\rvert^2 = 1, \lvert\Psi_2\rvert^2 = 1$	5 MW/cm^2, 10 MW/cm^2
$P = 1$	10 W

3. Numerical Results

3.1. Double Vortices States

The imaginary time method [55] was employed to obtain the stationary solutions of the normalized system of Equations (9) and (10), which is subjected to the phase matching conditions given by Equation (14). The stability of these solitons is then verified through real-time evolution. A random perturbation noise at a level of 0.1% was added during real-time evolution. Figure 1 presents typical examples of quasi-stable bright solitons produced with the phase-matching condition of a helical-periodically poled ferroelectric structure. Figure 1(a1,a2) show the intensity distributions of the FH and SH components of the solitons, respectively. The phase diagrams of the FH and SH components are displayed in Figure 1(b1,b2), respectively. The color distribution of the phase in Figure 1(b1,b2) exhibits a continuous rotation from red to blue, indicating that the FH and SH components of these solitons are vortex solitons. This implies that the helical-periodically poled scheme introduces a phase ϕ_d through QPM techniques, which is equivalent to embedding a topological charge (TC) in the crystal. The stability of these solitons is demonstrated in Figure 1(c1,c2), which show the results of direct simulations. The approximate stable propagation distance is 3.6 cm, which is sufficient for robust transmission in most commercially available crystals. In contrast, Figure 2(a1,a2) depict typical examples of bright solitons produced with the phase-matching condition of a nonhelical-periodically poled ferroelectric structure. In this case, without a helical-periodically poled ferroelectric structure, the bright vortex soliton cannot even be stably transmitted to 0.05 cm. This indicates that the phase-matching condition of a helical-periodically poled ferroelectric structure can greatly enhance the stability of bright vortex solitons. In contrast to the case where ϕ_d is a constant and cannot support stable vortex bright solitons, a helical-periodically poled structure can significantly improve their stability. This can be achieved by designing ϕ_d as a spatial function, particularly in a helical-periodically poled $LiNbO_3$ (HPPLN) crystal [50].

Figure 3 presents the characteristic curves of three key parameters, namely A_{eff}, β, and $I_{\max}$, plotted as functions of the input power (P) and effective detuning ($\Delta\Gamma$). Here, A_{eff} represents the effective area of the bright vortex solitons, β is the propagation constant, and $I_{\max}$ is the maximum light intensity. Notably, changes in P and $\Delta\Gamma$ have significant effects on A_{eff}, β, and $I_{\max}$.

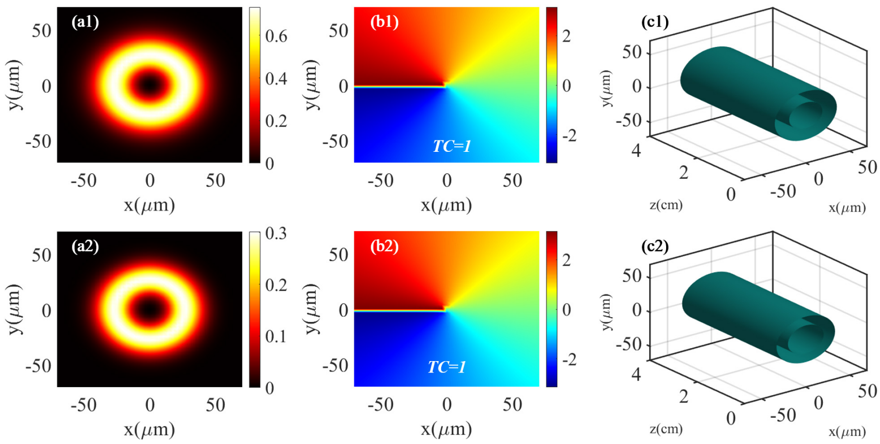

Figure 1. (Color online) Typical examples of quadratic solitons generated by quasi-phase matching in a helical-periodically poled ferroelectric crystal, HPPLN, with topological charges of two components, $S_1 = S_2 = +1$, respectively. (**a1**,**a2**) Intensity distributions of FH and SH components. (**b1**,**b2**) Phase diagrams of FH and SH components. (**c1**,**c2**) Stability of FH and SH components in a helical-periodically poled ferroelectric structure. The random perturbation noise of direct simulation is 0.1%. This soliton example is obtained with (P, $\Delta\Gamma$) = (300 W, 0 cm^{-1}).

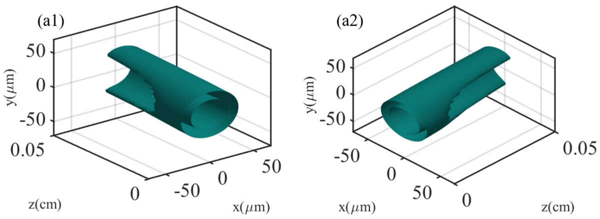

Figure 2. (Color online) Typical examples of quadratic solitons generated by quasi-phase matching in a nonhelical-periodically poled ferroelectric crystal, with topological charges of two components, $S_1 = S_2 = +1$, respectively. (**a1**,**a2**) Stability of the FH and the SH components. The random perturbation noise of direct simulation is 0.1%. This soliton example is produced by (P, $\Delta\Gamma$) = (300 W, 0 cm^{-1}).

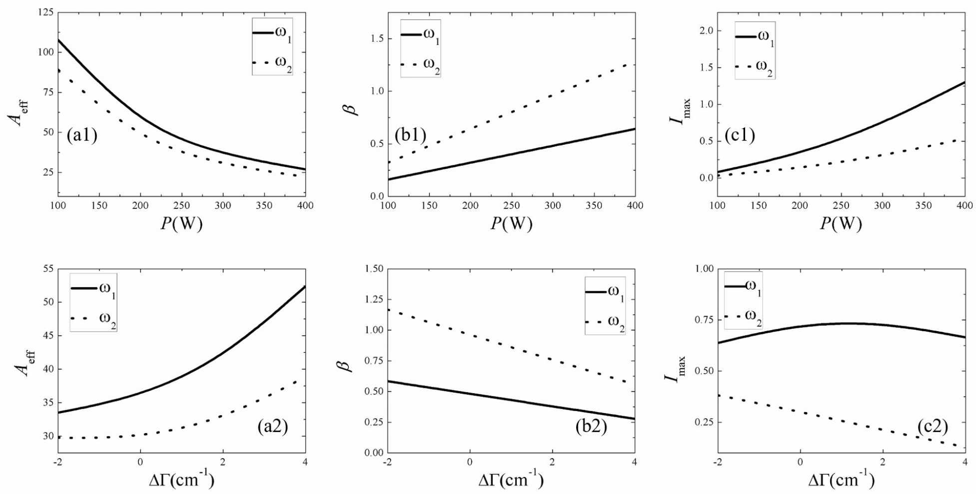

Figure 3. (Color online) The characteristics of $A_{\rm eff}$, β, and $I_{\rm max}$ with respect to P (**a1**,**b1**,**c1**) and $\Delta\Gamma$ (**a2**,**b2**,**c2**) are presented in this figure. The solid and dotted curves correspond to the FH and SH components of the solitons, respectively. All soliton solutions represented by the curves in those figures can stably propagate in the physical parameter space. The effective detuning $\Delta\Gamma$ = 0 cm^{-1} is fixed for the first row, while the input power P = 300 W is fixed for the second row.

In Figure 3(a1), the symbols ω_1 and ω_2 refer to the FH and SH components, respectively. Here, $A_{\rm eff}$ exhibits a decreasing trend with an increasing P and a fixed $\Delta\Gamma$ = 0 cm^{-1}. This decrease is due to the stronger self-focusing effect that occurs at higher powers, which causes the area of the solitons to shrink. Figure 3(b1) shows that $d\beta/dP > 0$, indicating that the vortex solitons satisfy the Vakhitov–Kolokolov (VK) criterion for stability in self-focusing media. This conclusion is verified by direct numerical simulations everywhere along this curve. Finally, in Figure 3(c1), $I_{\rm max}$ increases with P as expected.

The bottom row of Figure 3 depicts the relationship between $\Delta\Gamma$ and the three characteristic parameters. In Figure 3(a2), $A_{\rm eff}$ increases with $\Delta\Gamma$ when P = 300 W. However, if $\Delta\Gamma$ becomes too large (e.g., $\Delta\Gamma$ = 4 cm^{-1}), the QPM condition is not well satisfied, resulting in soliton expansion. Figure 3(b2) indicates that the propagation constant β decreases with increasing $\Delta\Gamma$. Finally, in Figure 3(c2), the $I_{\rm max}$ of the SH component decreases as $\Delta\Gamma$ increases, whereas the FH component initially increases and then decreases.

3.2. *Vortex–Antivortex States*

When the topological charges of the two components of a vortex soliton have opposite signs, a special mode known as the *vortex–antivortex* state is formed, where the vortices disappear due to the opposite topological charges carried by the two components. Figure 4 illustrates typical examples of the *vortex–antivortex* state. In Figure 4(b1,b2), the phase distributions of the vortex solitons are opposite, and the intensity distributions of the FH and SH components for the solitons are presented in Figure 4(a1,a2). The stability of the two components is displayed in Figure 4(c1,c2), indicating that the *vortex–antivortex* states can stably propagate in the physical parameter space. Figure 5(a1,a2) illustrate typical examples of bright solitons generated using the phase-matching condition of a nonhelical-periodically poled ferroelectric structure, which cannot be stably transmitted to 0.05 cm. Interestingly, under identical parameter conditions, the characteristic curves of $A_{\rm eff}$, β, and $I_{\rm max}$ versus P and $\Delta\Gamma$ exhibit degeneracy for both the *vortex–antivortex* states and *double vortices* states.

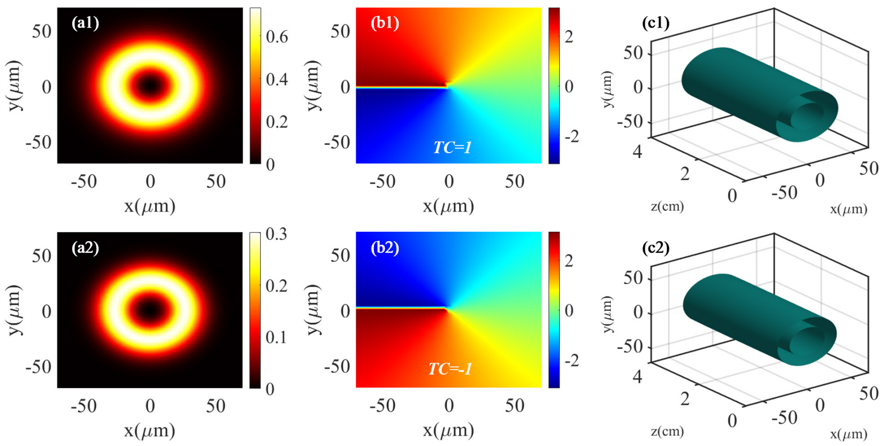

Figure 4. (Color online) Typical examples of quadratic solitons generated by quasi-phase matching in a helical-periodically poled ferroelectric crystal, HPPLN, with topological charges of two components are $S_1 = +1$ and $S_2 = -1$, respectively. (**a1**,**a2**) Intensity distributions of FH and SH components. (**b1**,**b2**) Phase diagrams of FH and SH components. (**c1**,**c2**) Stability of FH and SH components in a helical-periodically poled ferroelectric structure. The random perturbation noise of direct simulation is 0.1%. This soliton example is obtained with (P, $\Delta\Gamma$) = (300 W, 0 cm^{-1}).

The relationship between the input power P(W) and the stability propagation distance z(cm) of the solitons is investigated in Figure 6. As depicted in the figure, it is observed that as the input power P increases, the propagation distance z decreases. The stable propagation distance is a function of the power. For larger input powers, spatial solitons exhibit stronger nonlinear effects, leading to enhanced self-focusing and beam convergence. This results in the gradual contraction of the soliton during propagation, accompanied by an increase in its energy density. Consequently, the nonlinear effects are further intensified. As a consequence, the soliton experiences stronger nonlinear interactions, such as self-phase modulation and self-phase modulation-induced optical pumping, which distort the soliton and reduce its propagation distance. Thus, as the input power increases, the stable propagation distance of the soliton decreases. This finding suggests that utilizing lower input power may be advantageous in achieving vortex solitons with longer propagation distances.

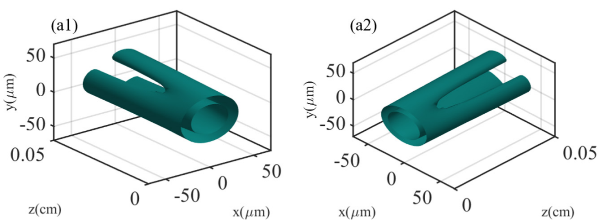

Figure 5. (Color online) Typical examples of quadratic solitons generated by quasi-phase matching in a nonhelical-periodically poled ferroelectric crystal, with topological charges of two components, $S_1 = +1$ and $S_2 = -1$, respectively. (**a1**,**a2**) Stability of the FH and the SH component. The random perturbation noise of direct simulation is 0.1%. This soliton example is produced by (P, $\Delta\Gamma$) = (300 W, 0 cm^{-1}).

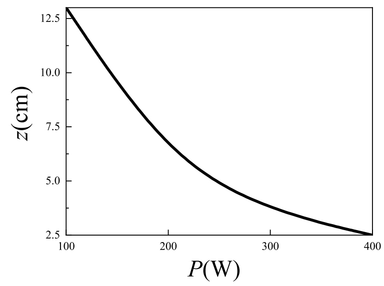

Figure 6. (Color online) The relationship diagram of the stable transmission distance z (cm) of optical vortex solitons for different actual powers P(W). The solitons consist of two components with topological charges of S = +1 each. Both components exhibit the same stability characteristics. The other parameter is $\Delta\Gamma = 0\ \mathrm{cm}^{-1}$.

4. Conclusions

The primary objective of this study is to employ ferroelectric crystals with helical-periodically poled structures to modulate quadratic bright vortex solitons using the QPM technique and achieve robust transmission of vortex solitons in pure $\chi^{(2)}$ nonlinear media in the actual parameter space. The theoretical model is based on the coupled equations of the second harmonic generation process under the slowly varying amplitude approximation. The modulation coefficient $d(r,\theta,z)$ in the equations represents the spatially varying magnitude of the $\chi^{(2)}$ susceptibility, which is expressed by a Fourier series expansion containing a modulation phase factor. By setting the modulation phase factor, the effect of embedding topological charges in the crystal is realized. Furthermore, the actual parameters of the model in the specific QPM material $LiNbO_3$ are discussed, and the conversion relationship between dimensionless units and physical units is presented. By taking different values of n, different lowest value solutions generated by different modulation phase factors are discussed, and two kinds of lowest vortex states are condensed: *double vortices* state and *vortex–antivortex* state (*hidden vortices* is a special type of *vortex–antivortex* state). In the numerical results section, the intensity distributions, phase diagrams, and real-time evolution stability of the bright vortex solitons obtained in the *double vortices* states and *vortex–antivortex* states are discussed. The dependence of three characteristic parameters, effective area A_{eff}, propagation constant β, and maximum light intensity I_{max}, on the input power P and effective detuning $\Delta\Gamma$ are studied numerically. The two states are characterized by degeneracy. The real-time evolution results demonstrate that vortex solitons can be stably transmitted for 3.6 cm in the quasi-phase matching-modulated crystal with helical-periodically poled structures, exceeding most commercially available crystals. In contrast, if in a crystal with a nonhelical-periodically poled structure, vortex solitons cannot even be stably transmitted to 0.05 cm. This result demonstrates that the azimuthal modulation instability of vortex solitons can be effectively overcome under these conditions, providing a novel solution for the quasi-stable transmission of bright vortex solitons.

It would be intriguing to extend this research to *vortex–antivortex* with higher angular momentum. A challenging yet promising possibility is to investigate a vortex soliton with a smaller topological charge embedded in a vortex soliton with a larger topological charge, resulting in a novel state known as a *nested vortex*.

Author Contributions: Conceptualization, methodology, software, visualization, Y.C. and A.Y.; writing—original draft preparation, Y.C.; writing—review and editing, Y.C., Y.Z., and H.H.; supervision, project administration, H.H.; funding acquisition, Y.Z. and J.X. All authors have read and agreed to the published version of the manuscript.

Funding: This research was funded by the NNSFC (China) grant numbers 12274077, 11874112, 11905032, 62005044, by the Guangdong Basic and Applied Basic Research Foundation through grant Nos. 2021A1515111015, 2019A1515110924, the Key Research Projects of General Colleges in Guangdong Province through grant No. 2019KZDXM001, the Research Fund of Guangdong-Hong

Kong-Macao Joint Laboratory for Intelligent Micro-Nano Optoelectronic Technology through grant No.2020B1212030010 and the Graduate Innovative Talents Training Program of the Foshan University.

Institutional Review Board Statement: Not applicable.

Informed Consent Statement: Not applicable.

Data Availability Statement: The data is available from the corresponding author upon request.

Acknowledgments: Throughout the writing of this dissertation I have received a great deal of support and assistance. I would first like to thank one of my supervisors, Yongyao Li, whose expertise was invaluable in formulating the research questions and methodology. Your insightful feedback pushed me to sharpen my thinking and brought my work to a higher level.

Conflicts of Interest: The authors declare no conflict of interest.

Abbreviations

The following abbreviations are used in this manuscript:

QPM	Quasi-Phase Matching
FF	Fundamental Frequency
SH	Second Harmonic
BECs	Bose–Einstein Condensates

References

1. Fedotova, A.; Younesi, M.; Sautter, J.; Vaskin, A.; Löchner, F.J.F.; Steinert, M.; Geiss, R.; Pertsch, T.; Staude, I.; Setzpfandt, F. Second-Harmonic Generation in Resonant Nonlinear Metasurfaces Based on Lithium Niobate. *Nano Lett.* **2020**, *20*, 8608–8614. [CrossRef] [PubMed]
2. Tang, F.; Ohto, T.; Sun, S.; Rouxel, J.R.; Imoto, S.; Backus, E.H.G.; Mukamel, S.; Bonn, M.; Nagata, Y. Molecular Structure and Modeling of Water-Air and Ice-Air Interfaces Monitored by Sum-Frequency Generation. *Chem. Rev.* **2020**, *120*, 3633–3667. [CrossRef] [PubMed]
3. Zhang, K.; Wang, W.; Liu, S.S.; Pan, X.Z.; Du, J.J.; Lou, Y.B.; Yu, S.; Lv, S.C.; Treps, N.; Fabre, C.; et al. Reconfigurable Hexapartite Entanglement by Spatially Multiplexed Four-Wave Mixing Processes. *Phys. Rev. Lett.* **2020**, *124*, 090501. [CrossRef]
4. Stolen, R.H.; Bösch, M.A.; Lin, C. Phase matching in birefringent fibers. *Opt. Lett.* **1981**, *6*, 213–215. [CrossRef] [PubMed]
5. Fiore, A.; Janz, S.; Delobel, L.; Van der Meer, P.; Bravetti, P.; Berger, V.; Rosencher, E.; Nagle, J. Second-harmonic generation at λ= 1.6 μm in AlGaAs/Al_2O_3 waveguides using birefringence phase matching. *Appl. Phys. Lett.* **1998**, *72*, 2942–2944. [CrossRef]
6. Zhang, B.; Li, L.Q.; Wang, L.; Chen, F. Second harmonic generation in femtosecond laser written lithium niobate waveguides based on birefringent phase matching. *Opt. Mater.* **2020**, *107*, 110075. [CrossRef]
7. Boyd, R.W. *Nonlinear Optics*; Academic: New York, NY, USA, 2008; pp. 69–104.
8. Armstrong, J.A.; Bloembergen, N.; Ducuing, J.; Pershan, P.S. Interactions between light waves in a nonlinear dielectric. *Phys. Rev.* **1962**, *127*, 1918. [CrossRef]
9. Arie A; Voloch, N. Periodic, quasiperiodic and random quadratic nonlinear photonic crystals. *Laser Photonics Rev.* **2010**, *4*, 355–373. [CrossRef]
10. Li, H.; Ma, B. Research development on fabrication and optical properties of nonlinear photonic crystals. *Front. Optoelectron.* **2020**, *13*, 35–49. [CrossRef]
11. Yamada, M.; Nada, N.; Saitoh, M.; Watanabe, K. First-order quasi-phase matched $LiNbO_3$ waveguide periodically poled by applying an external field for efficient blue second-harmonic generation. *Appl. Phys. Lett.* **1993**, *62*, 435–436. [CrossRef]
12. Myers, L.E.; Eckardt, R.C.; Fejer, M.M.; Byer, R.L.; Bosenberg, W.R.; Pierce, J.W. Quasi-phase-matched optical parametric oscillators in bulk periodically poled $LiNbO_3$. *J. Opt. Soc. Am. B* **1995**, *12*, 2102–2116. [CrossRef]
13. Zhu, S.N.; Zhu, Y.Y.; Ming, N.B. Quasi-phase-matched third-harmonic generation in a quasi-periodic optical superlattice. *Science* **1997**, *278*, 843–846. [CrossRef]
14. Arie A; Bahabad A; Habshoosh N. Nonlinear interactions in periodic and quasi-periodic nonlinear photonic crystals. *Ferroelectric Crystals for Photonic Applications: Including Nanoscale Fabrication and Characterization Techniques*; Springer: Berlin/Heidelberg, Germany, 2009; pp. 259–284.
15. Wei, D.Z.; Wang, C.W.; Xu, X.Y.; Wang, H.J.; Hu, Y.L.; Chen, P.C.; Li, J.W.; Zhu, Y.Z.; Xin, C.; Hu, X.P.; et al. Efficient nonlinear beam shaping in three-dimensional lithium niobate nonlinear photonic crystals. *Nat. Commun.* **2019**, *10*, 4193. [CrossRef]
16. Chiang, A.C.; Chao, J.H.; Lin, S.T.; Lin, Y.Y. Observation of Neutron-Induced Absorption and Phase-Mismatch for Quasi-Phase-Matched Second Harmonic Generation in Congruent Lithium Niobate. *Photonics* **2022**, *9*, 225. [CrossRef]
17. Sabirov, O.I.; Assanto, G.; Sapaev, U.K. Efficient Third-Harmonic Generation by Inhomogeneous Quasi-Phase-Matching in Quadratic Crystals. *Photonics* **2022**, *10*, 76. [CrossRef]

18. Lai, P.; Chang, C.; Liu, X.; Wei, D. Multiplexing Linear and Nonlinear Bragg Diffractions through Volume Gratings Fabricated by Femtosecond Laser Writing in Lithium Niobate Crystal. *Photonics* **2023**, *10*, 562. [CrossRef]
19. Jia, R.; Liu, M.; Liu, J.M.; Hua, P.R.; Zhang, D.L. A Theoretical Study on Mid-Infrared Difference Frequency Generation Based on Periodically Poled Thin-Film $LiNbO_3$. *Photonics* **2023**, *10*, 478. [CrossRef]
20. Torner, L.; Stegeman, G.I. Soliton evolution in quasi-phase-matched second-harmonic generation. *J. Opt. Soc. Am. B* **1997**, *14*, 3127–3133. [CrossRef]
21. Clausen, C.B.; Bang, O.; Kivshar, Y.S. Spatial solitons and induced Kerr effects in quasi-phase-matched quadratic media. *Phys. Rev. Lett.* **1997**, *78*, 4749–4752. [CrossRef]
22. Desyatnikov, A.S.; Torner, L.; Kivshar, Y.S. Optical Vortices and Vortex Solitons. *Prog. Opt.* **2005**, *47*, 291–391.
23. Malomed, B.A. Vortex solitons: Old results and new perspectives. *Phys. D* **2019**, *399*, 108–137. [CrossRef]
24. Grier, D.G. A revolution in optical manipulation. *Nature* **2003**, *424*, 810–816. [CrossRef] [PubMed]
25. Curtis, J.E.; Koss, B.A.; Grier, D.G. Dynamic holographic optical tweezers. *Opt. Commun.* **2002**, *207*, 169–175. [CrossRef]
26. Vaziri, A.; Pan, J. W.; Jennewein, T.; Weihs, G.; Zeilinger, A. Concentration of higher dimensional entanglement: Qutrits of photon orbital angular momentum. *Phys. Rev. Lett.* **2003**, *91*, 227902. [CrossRef] [PubMed]
27. Molina-Terriza, G.; Torres, J.P.; Torner, L. Twisted photons. *Nat. Phys.* **2007**, *3*, 305–310. [CrossRef]
28. Molina-Terriza, G.; Vaziri, A.; Rehacek, J.; Hradil, Z.; Zeilinger, A. Triggered qutrits for quantum communication protocols. *Phys. Rev. Lett.* **2004**, *92*, 167903. [CrossRef]
29. Etrich, C.; Lederer, F.; Malomed, B.A.; Peschel, T.; Peschel, U. Optical solitons in media with a quadratic nonlinearity. *Prog. Opt.* **2000**, *41*, 483–568.
30. Buryak, A.V.; Trapani, P.D.; Skryabin, D.V.; Trillo, S. Optical solitons due to quadratic nonlinearities: From basic physics to futuristic applications. *Phys. Rep*. **2002**, *370*, 63–235. [CrossRef]
31. Torruellas, W.E.; Wang, Z.; Hagan, D.J.; VanStryland, E.W.; Stegeman, G.I.; Torner, L.; Menyuk, C.R. Observation of Two-Dimensional Spatial Solitary Waves in a Quadratic Medium. *Phys. Rev. Lett*. **1995**, *74*, 5036–5039. [CrossRef]
32. Torruellas, W.E.; Wang, Z.; Torner, L.; Stegeman, G.I. Observation of mutual trapping and dragging of two-dimensional spatial solitary waves in a quadratic medium. *Opt. Lett*. **1995**, *20*, 1949–1951. [CrossRef]
33. Torner, L.; Petrov, D.V. Azimuthal instabilities and self-breaking of beams into sets of solitons in bulk second-harmonic generation. *Electron. Lett*. **1997**, *33*, 608–609. [CrossRef]
34. Firth W.J.; Skryabin, D.V. Optical solitons carrying orbital angular momentum. *Phys. Rev. Lett*. **1997**, *79*, 2450–2453. [CrossRef]
35. Petrov, D.V.; Torner, L.; Martorell, J.; Vilaseca, R.; Torres, J.P.; Cojocaru, C. Observation of azimuthal modulational instability and formation of patterns of optical solitons in a quadratic nonlinear crystal. *Opt. Lett.* **1998**, *23*, 1444–1446. [CrossRef]
36. Mihalache, D.; Mazilu, D.; Crasovan, L.-C.; Towers, I.; Buryak, A.V.; Malomed, B.A.; Torner, L.; Torres, J.P.; Lederer, F. Stable spinning optical solitons in three dimensions. *Phys. Rev. Lett.* **2002**, *88*, 073902. [CrossRef]
37. Mihalache, D.; Mazilu, D.; Malomed, B.A.; Lederer, F. Stable vortex solitons in a vectorial cubic-quintic model. *J. Opt. B* **2004**, *6*, S341–S350. [CrossRef]
38. Mihalache, D.; Mazilu, D.; Towers, I.; Malomed, B.A.; Lederer, F. Stable two-dimensional spinning solitons in a bimodal cubic-quintic model with four-wave mixing. *J. Opt. A* **2002**, *4*, 615–623. [CrossRef]
39. Towers, I.; Buryak, A.V.; Sammut, R.A.; Malomed, B.A. Stable localized vortex solitons. *Phys. Rev. E* **2001**, *63*, 055601. [CrossRef]
40. Mihalache, D.; Mazilu, D.; Malomed, B.A.; Lederer, F. Stable vortex solitons supported by competing quadratic and cubic nonlinearities. *Phys. Rev. E* **2004**, *69*, 066614. [CrossRef] [PubMed]
41. Di Trapani, P.; Chinaglia, W.; Minardi, S.; Piskarskas, A. Observation of quadratic optical vortex solitons. *Phys. Rev. Lett* **2000**, *84*, 3843–3846. [CrossRef]
42. Kartashov, Y.V.; Malomed, B.A.; Tarruell, L.; Torner, L. Three-dimensional droplets of swirling superfluids. *Phys. Rev. A* **2018**, *98*, 013612. [CrossRef]
43. Li, Y.Y.; Chen, Z.P.; Luo, Z.H.; Huang, C.Q.; Tan, H.S.; Pang, W.; Malomed, B.A. Two-dimensional vortex quantum droplets. *Phys. Rev. A* **2018**, *98*, 063602. [CrossRef]
44. Luo, Z.H.; Pang, W.; Liu, B.; Li, Y.Y.; Malomed, B.A. A new form of liquid matter: Quantum droplets. *Front. Phys.* **2021**, *16*, 1–21. [CrossRef]
45. Petrov, D.S. Quantum mechanical stabilization of a collapsing Bose-Bose mixture. *Phys. Rev. Lett.* **2015**, *115*, 155302. [CrossRef] [PubMed]
46. Petrov, D.S.; Astrakharchik, G.E. Ultradilute low-dimensional liquids. *Phys. Rev. Lett* **2016**, *117*, 100401. [CrossRef]
47. Lobanov, V.E.; Kalinovich, A.A.; Borovkova, O.V.; Malomed, B.A. Fundamental and vortex dissipative quadratic solitons supported by spatially localized gain. *Phys. Rev. A* **2022**, *105*, 013519. [CrossRef]
48. Zhao, F.Y.; Xu, X.X.; He, H.X.; Zhang, L.; Zhou, Y.G.; Chen, Z.P.; Malomed, B.A.; Li, Y.Y. Vortex solitons in quasi-phase-matched photonic crystals. *Phys. Rev. Lett.* **2023**, *130*, 157203. [CrossRef]
49. Bahabad, A.; Arie, A. Generation of optical vortex beams by nonlinear wave mixing. *Opt. Express* **2007**, *15*, 17619–17624. [CrossRef]
50. Tian, L.H.; Ye, F.W.; Chen, X.F. Optical vortex converter with helical-periodically poled ferroelectric crystal. *Opt. Express* **2011**, *19*, 11591–11596. [CrossRef]
51. Phillips, C.R.; Langrock, C.; Chang, D.; Lin, Y.W.; Gallmann, L.; Fejer, M.M. Apodization of chirped quasi-phasematching devices. *J. Opt. Soc. Am. B* **2013**, *30*, 1551–1568. [CrossRef]

52. Zhao, F.Y.; Lü, J.T.; He, H.X.; Zhou, Y.G.; Fu, S.H.; Li, Y.Y. Geometric phase with full-wedge and half-wedge rotation in nonlinear frequency conversion. *Opt. Express* **2021**, *29*, 21820–21832. [CrossRef]
53. Porat, G.; Arie, A. Efficient, broadband, and robust frequency conversion by fully nonlinear adiabatic three-wave mixing. *J. Opt. Soc. Am. B* **2013**, *30*, 1342–1351. [CrossRef]
54. Chen, Y.X.; Cai, X.Y.; Liu, B.; Jiang, X.D.; Li, Y.Y. Hidden vortices of quantum droplets in quasi-two dimensional space. *Acta Phys. Sin.* **2022**, *71*, 200302. [CrossRef]
55. Yang, J.K.; Lakoba, T.I. Universally-convergent squared-operator iteration methods for solitary waves in general nonlinear wave equations. *Stud. Appl. Math* **2008**, *120*, 265–292. [CrossRef]